

# Sphinx: EFFICIENTLY SERVING NOVEL VIEW SYNTHESIS USING REGRESSION-GUIDED SELECTIVE REFINEMENT

Yuchen Xia<sup>1</sup> Souvik Kundu<sup>2</sup> Mosharaf Chowdhury<sup>3</sup> Nishil Talati<sup>1,3</sup>

## ABSTRACT

Novel View Synthesis (NVS) is the task of generating new images of a scene from viewpoints that were not part of the original input. Diffusion-based NVS can generate *high-quality*, temporally consistent images, however, remains computationally prohibitive. Conversely, regression-based NVS offers suboptimal generation quality despite requiring *significantly lower compute*; leaving the design objective of a high-quality, inference-efficient NVS framework an open challenge. To close this critical gap, we present **Sphinx**, a *training-free hybrid inference framework* that achieves *diffusion-level fidelity at a significantly lower compute*. Sphinx proposes to use regression-based *fast initialization* to guide and reduce the denoising workload for the diffusion model. Additionally, it integrates *selective refinement* with adaptive noise scheduling, allowing more compute to uncertain regions and frames. This enables Sphinx to provide *flexible navigation of the performance-quality trade-off*, allowing adaptation to latency and fidelity requirements for *dynamically changing* inference scenarios. Our evaluation shows that Sphinx achieves an average **1.8×** speedup over diffusion model inference with negligible perceptual degradation of less than 5%, establishing a new Pareto frontier between quality and latency in NVS serving. Code is available at: <https://github.com/stsxxx/Sphinx>.

## 1 INTRODUCTION

NVS aims to generate unseen viewpoints of a scene from any number of input images and has recently attracted significant attention in AR/VR, 3D reconstruction, and free-viewpoint video applications (Zhang et al., 2025b; Cai & Lu, 2024). Based on the model design, NVS methods can be classified into two categories: regression-based and diffusion-based (Berian & Mahalanobis, 2025). Regression models predict target views directly from scene geometry in a single feed-forward pass, achieving real-time performance but often yielding oversmoothed results. Diffusion-based models leverage strong generative priors to synthesize high-fidelity, temporally consistent views through iterative denoising, which comes with high computational cost. These two families embody a fundamental trade-off between speed and visual quality.

Recent advances in efficient inference have shown that combining models of different capacities can effectively balance quality and latency. Prior works such as speculative decoding and others (Leviathan et al., 2023; Xia et al., 2026; Miao et al., 2024; Yang et al., 2024) have explored combining different types of models to achieve faster responses while maintaining comparable quality across various tasks. These

<sup>1</sup>University of Illinois Urbana-Champaign, Illinois, USA <sup>2</sup>Intel AI Group, USA <sup>3</sup>University of Michigan, Michigan, USA. Correspondence to: Yuchen Xia <yxia28@illinois.edu>.

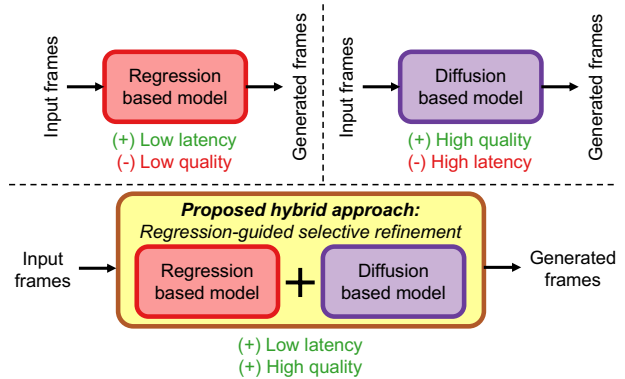


Figure 1. Overview of Sphinx that combines regression and diffusion models for low-latency, high-quality generation.

methods are training-free, relying solely on system-level design to coordinate models of different strengths at inference. Inspired by their successes, we investigate whether a similar hybrid strategy can benefit NVS. Given the trade-off between regression and diffusion-based models, a key question is: *how can we effectively combine multiple models to achieve the best of both worlds: high fidelity and efficiency?*

In this paper, we present a hybrid framework called Sphinx that combines the efficiency of regression models with the fidelity of diffusion models, as shown in Figure 1. Our approach first uses a regression model for fast initialization to predict coarse target views, effectively reducing the number of denoising steps required in the subsequent diffusion refinement stage. It further integrates selective refinement

with partial denoising, applying diffusion only to regions or frames that require higher-quality reconstruction, which enables adaptive allocation of computation based on scene complexity. To fully leverage this design, several **challenges** must be addressed: (1) selecting appropriate noise levels to balance efficiency and quality, (2) preserving temporal and spatial consistency under partial refinement, (3) performing sparse spatial refinement efficiently, and (4) adaptively balancing quality and performance across diverse scenes.

To address these challenges, we propose the following solutions. First, we introduce an adaptive noise scheduling strategy that dynamically selects denoising starting points based on the confidence of regression outputs. Second, we introduce a latent cache mechanism that periodically caches intermediate features from attention layers to ensure spatial and temporal consistency while avoiding redundant computation. Third, we employ block-based sparse convolution to enable efficient and selective refinement. Finally, we use a CLIP-based clustering module to adaptively select refinement logic and noise scheduling during inference.

We evaluate our approach on three diverse datasets: RE10K (Zhou et al., 2018), DL3DV (Ling et al., 2024) and ACID (Liu et al., 2021), using SEVA (Gao et al.) and ViewCrafter (Yu et al., 2025) as representative diffusion-based NVS models. Our experiments assess visual quality using MUSIQ (Ke et al., 2021), LPIPS (Zhang et al., 2018), PSNR, and SSIM (Wang et al., 2004), along with efficiency metrics such as average and tail latency. Across all datasets, Sphinx achieves up to  $2.7\times$  speedup over full diffusion inference while maintaining comparable visual quality. The trade-off space between quality and latency further shows that Sphinx resides on the Pareto frontier, demonstrating its ability to achieve an optimal balance between fidelity and efficiency. The contributions of Sphinx are as follows:

- A hybrid NVS pipeline that initializes diffusion-based refinement with regression-based predictions, reducing the computational complexity of the workload.
- An efficient sparsity-aware refinement scheme that restricts diffusion computation to uncertain regions.
- An adaptive mechanism for denoising-step decision logic that dynamically determines how many diffusion steps can be skipped per frame.
- A system design that achieves up to  $2.2\times$  speedup with less than 5% degradation in perceptual quality.

## 2 BACKGROUND AND MOTIVATION

### 2.1 Novel View Synthesis (NVS)

NVS aims to generate unseen views of a scene from a limited set of input images with known camera (Liu et al., 2025). The goal is to produce geometrically consistent and photorealistic renderings from novel viewpoints, or along



Figure 2. Example NVS task: two input camera frames are used to generate four intermediate novel views between them.

a smooth camera trajectory to form a temporally coherent video sequence. Figure 2 illustrates an example NVS task, where two input views synthesize intermediate frames. NVS is a core problem in vision and graphics, with applications in 3D reconstruction, AR/VR, and immersive media creation.

The main challenge is jointly modeling scene geometry and appearance to render realistic new views. Traditional methods based on explicit geometry and image-based rendering often fail under occlusions or sparse inputs, while modern neural approaches learn implicit or generative representations end-to-end, achieving photorealistic and view-consistent results from limited observations.

### 2.2 NVS Algorithms and Models

Existing NVS approaches can be broadly grouped into **regression-based** and **diffusion-based** models, depending on how they map input views to unseen target views.

**Regression-based models** learn a deterministic mapping from input images and camera poses to target views, directly predicting color and geometry. Classic NeRF models (Mildenhall et al., 2020) represent scenes as continuous 3D fields optimized per scene, achieving high geometric accuracy but requiring dense inputs and expensive optimization. Recent feed-forward regressors such as MVSplat (Chen et al., 2024), PixelSplat (Charatan et al., 2024), and DepthSplat (Xu et al., 2025) remove per-scene training and achieve real-time rendering by splatting 3D Gaussians or depth features to target viewpoints. However, these methods often degrade under sparse inputs and lose fine details during large viewpoint changes.

**Diffusion-based models** instead learn a generative distribution over target views conditioned on observed inputs and camera parameters. Leveraging strong image and video diffusion priors, methods such as MotionCtrl (Wang et al., 2024c), ViewCrafter (Yu et al., 2025), and SEVA (Gao et al.) can synthesize high-quality, temporally consistent views even from extremely sparse inputs. Their generative nature makes them highly robust and generalizable, but the iterative denoising process introduces substantial computational overhead compared to regression-based approaches.

### 2.3 Performance-Quality Trade-off

Regression-based methods emphasize geometric accuracy and computational efficiency, whereas diffusion-based approaches focus on perceptual realism and robustness under

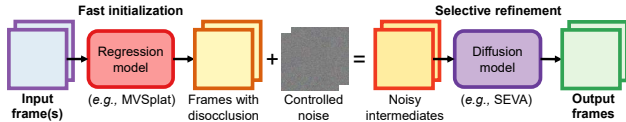


Figure 3. Proposed hybrid approach combining regression-based fast initialization with diffusion-based selective denoising.

sparse-view conditions. In recent regression-based models (Chen et al., 2024; Zhang et al., 2025a; Wang et al., 2024b), a lightweight neural network first extracts 2D feature maps from the input images, lifts them into 3D Gaussians, and then applies Gaussian splatting to project these features into the target viewpoint, enabling fast and feed-forward novel view synthesis. Diffusion-based models, on the other hand, adopt an iterative denoising process in which each timestep refines the latent representation of the target view through a full network pass (You et al., 2025; Watson et al., 2024). This progressive refinement allows them to recover high-frequency details and improve perceptual fidelity, but it also introduces substantial computational overhead and latency compared to the single-pass regression pipeline. Overall, these two model families embody a *fundamental trade-off* in NVS: diffusion models achieve superior quality at the cost of speed, while regression models provide real-time inference but often sacrifice quality.

In our experiments on an NVIDIA A40 GPU, the diffusion-based SEVA model takes over **80 seconds** to generate 19 novel views, while the regression-based MVSpIat completes the same task in just **5 seconds**: a speedup of more than **16×**. In terms of perceptual quality, images generated by MVSpIat achieve a MUSIQ score (Ke et al., 2021) of around **55**, whereas SEVA reaches approximately **65**. This disparity underscores the quality–performance trade-off, raising the following research question: *How can we combine the efficiency of regression-based methods with the generative strength of diffusion models?*

### 3 PROPOSAL: A HYBRID APPROACH

To balance complementary strengths from regression and diffusion models, we propose to integrate both paradigms into a *hybrid generation pipeline*. As illustrated in Figure 3, our design is built around a two-stage hybrid inference process. We first employ a regression model to produce an initial estimate that captures the global scene structure, depth consistency, and coarse appearance. This serves as a strong prior for the subsequent diffusion process. Instead of starting from Gaussian noise, the diffusion model initializes from the regression output, to which we inject some amount of controlled noise; it then performs *partial denoising* to remove only this added noise and residual artifacts, refining high-frequency details and restoring fine textures while requiring far fewer steps than full denoising. By leveraging

a fast, deterministic regression output as the starting point, our hybrid approach substantially reduces the number of diffusion steps needed to achieve high-quality synthesis while maintaining temporal and spatial coherence.

To further improve efficiency, we introduce *selective refinement*, where only parts of the regression output that require improvement are processed by the diffusion model. Instead of refining the entire image, we identify low-confidence regions such as disoccluded areas, specular highlights, or motion-blurred regions using metrics like predicted opacity or blur detection algorithms. These regions are then selectively denoised through diffusion, while reliable regions from the regression output are preserved unchanged. This sparse refinement strategy ensures that diffusion operates only where necessary, further reducing computational overhead while maintaining high perceptual quality.

Through this design, we achieve the best of both worlds: the speed close to regression-based models and the realism of diffusion-based generation. The combination of fast initialization and selective refinement greatly reduces the denoising workload while preserving fine perceptual details in the most visually critical regions.

### 4 DESIGN CHALLENGES AND GOALS

While the hybrid approach outlined above is effective at a high level, fully realizing its benefits requires addressing several key design challenges, which we detail below.

**Challenge 1: Adaptive noise injection for regression outputs.** A primary challenge lies in determining the appropriate amount of noise to add to each regression output before invoking the diffusion model for refinement. The required noise level varies not only across different scenes but also across individual frames within the same scene, depending on texture richness, motion magnitude, and lighting conditions.

Moreover, target frames that are temporally distant from the input or reference views often exhibit larger geometric disparities and reconstruction errors, resulting in lower-quality regression outputs that demand stronger refinement. Consequently, a uniform noise level is suboptimal: insufficient noise leaves artifacts and residual blur unrefined, while excessive noise increases computational cost and risks over-smoothing fine details. The system must therefore not only adaptively infer the required noise level (or equivalently, the starting denoising step) for each frame and scene, but also develop a reliable way to quantify the quality of each regression output, measuring how far it deviates from the desired perceptual quality, and use this metric to determine the appropriate amount of noise to inject.

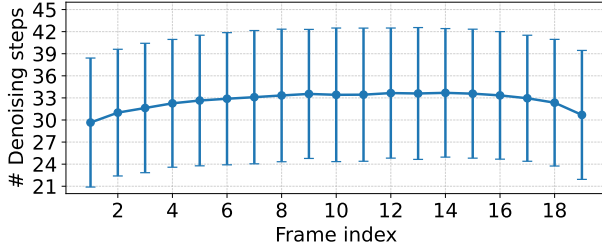


Figure 4. Number of denoising steps for each target frame in our pipeline on the RE10K dataset, with error bars indicating variability across scenes.

**Design Goal (DG1):** Adaptively determine the noise level for each regression output based on its predicted quality, injecting only as much noise as needed to balance refinement fidelity and efficiency.

**Challenge 2: Maintaining temporal consistency under partial denoising.** Diffusion-based NVS models typically process a batch of temporally adjacent frames jointly to preserve cross-frame consistency. In these models, each transformer block includes a temporal attention layer that captures motion cues and correspondences across neighboring frames, ensuring temporal coherence in the generated sequence. However, partial denoising breaks this assumption: only frames requiring refinement are processed at each timestep, while others are skipped. This selective participation disrupts the temporal attention mechanism and can lead to inconsistent motion, flickering, or misaligned structures across frames.

As shown in Figure 4, the number of denoising steps varies across target frames, indicating differing refinement requirements. This variation arises because target frames farther from the input views typically involve larger viewpoint changes and thus require more generative denoising steps. The challenge, therefore, lies in designing a mechanism that preserves temporal coherence even when only a subset of frames is refined: maintaining consistent temporal relationships and visual stability while still achieving substantial computational savings.

**Design Goal (DG2):** Maintain temporal coherence during partial denoising by preserving motion and structural consistency, even when only a subset of frames is refined.

**Challenge 3: Efficient sparse refinement within frames.** Not all pixels within a frame require equal refinement: regions that remain visually consistent across views or exhibit high-confidence regression outputs (e.g., low uncertainty, low motion, or smooth opacity) can be directly reused from



Figure 5. Qualitative comparison between regression output (MVSplat) and ground truth. The regression outputs contain disoccluded regions (highlighted in red) where artifacts and missing details appear, while the remaining regions are clean and consistent.

the regression results. In contrast, disoccluded or unobserved regions often contain artifacts, noise, or missing details that require generative refinement. As illustrated in Figure 5, these low-quality regions typically occupy only a small portion of the image, while most other areas are clean and consistent.

This motivates a sparse refinement strategy where diffusion focuses computation only on uncertain, degraded, or newly revealed content rather than the entire frame. However, identifying which regions are of low quality is itself challenging, as it requires a reliable measure of spatial confidence or perceptual degradation that can be estimated online without ground truth. Even after such regions are identified, selectively refining only part of a frame introduces spatial sparsity, which is difficult for existing diffusion architectures.

Convolutional and attention layers in these models are optimized for dense, contiguous feature maps, and operating on irregularly distributed pixels or small disjoint patches leads to significant memory overhead and inefficient GPU utilization. Furthermore, unstructured sparsity disrupts local feature aggregation and neighborhood coherence, which are crucial for accurate denoising. The challenge is to design an efficient sparse refinement mechanism that can both identify and refine low-quality regions while preserving spatial context and reducing redundant computation.

**Design Goal (DG3):** Enable effective, spatially selective refinement that concentrates computation on uncertain regions while preserving spatial correlations for coherent visual quality.

**Challenge 4: Adaptive decision logic for varying scene characteristics.** A single static denoising configuration cannot generalize across diverse scenes or workloads. The optimal balance between quality and efficiency depends on multiple factors such as scene complexity, motion magnitude, and target fidelity. Different scenes exhibit distinct characteristics: indoor scenes often contain limited depth variation, controlled lighting, and more structured geometry, while outdoor scenes tend to have larger depth ranges, dynamic illumination, and complex textures.

Moreover, variations in camera intrinsics and extrinsics across different scenes or sequences introduce further diversity in viewpoint distribution and projection geometry, affecting both the regression accuracy and the difficulty of diffusion-based refinement. These variations make a fixed denoising policy inadequate, as the ideal number of steps and spatial refinement regions can differ substantially between scenes. The challenge is therefore to develop an adaptive decision logic that dynamically adjusts denoising steps and refinement scope based on scene content and camera configuration, enabling fine-grained control over the quality-performance trade-off and ensuring robust operation under diverse real-world settings.

***Design Goal (DG4):** Adaptively balance quality and performance by adjusting denoising steps and refinement scope based on scene complexity and viewing conditions.*

## 5 Sphinx SYSTEM DESIGN

This section presents the overall design of **Sphinx**, our hybrid regression-diffusion framework by addressing the challenges discussed in §4.

### 5.1 Adaptive Noise Scheduling

To address **Challenge 1**, Sphinx employs an adaptive noise scheduling strategy that balances efficiency and quality. Sphinx enforces a *quality target* to ensure that the refined output maintains perceptual fidelity comparable to full diffusion while avoiding redundant computation. Let  $Q_{\text{full}}$  denote the perceptual quality of an image produced by full diffusion, and let  $Q_{\text{Sphinx}}(k)$  represent the quality of our output when refinement begins at denoising step  $k$ . We define a quality constraint as

$$Q_{\text{Sphinx}}(k) \geq \alpha \cdot Q_{\text{full}}, \quad 0 < \alpha \leq 1, \quad (1)$$

which ensures that each generated frame achieves at least a fraction  $\alpha$  of the perceptual quality of a pure diffusion model. For example, when  $\alpha = 0.95$ , the system aims for the refined output to reach at least 95% of the visual quality of an image fully generated by diffusion.

To determine how much noise to add, we require a metric that can estimate image quality online during inference. Traditional full-reference metrics such as SSIM or PSNR are unsuitable for this purpose because they require access to ground-truth images, which are unavailable during generation. Therefore, Sphinx adopts a non-reference image quality metric, MUSIQ (Ke et al., 2021), which predicts perceptual quality from visual content alone.

Using MUSIQ, we can obtain a quality score  $\hat{Q}_{\text{reg}}$  for each regression output. However, since each scene exhibits a different range of MUSIQ scores depending on its content and lighting conditions, the absolute score of a regression output alone is insufficient to determine its relative quality. Therefore, we evaluate the quality of each regression output using the ratio between its MUSIQ score and the reference quality, which reflects how close the regression result is to the desired perceptual fidelity. However, because ground-truth target images are unavailable during inference, the reference quality cannot be measured directly. To approximate it, Sphinx leverages the input views: we compute their MUSIQ scores and interpolate them to estimate the expected reference quality for each target frame. We adopt a power-based interpolation function to capture smooth variation in perceptual quality across viewpoints:

$$Q^* = c_0 + (c_1 - c_0) \cdot f(t),$$

$$f(t) = \begin{cases} t^\gamma, & c_1 \geq c_0, \\ 1 - (1 - t)^\gamma, & c_1 < c_0, \end{cases} \quad (2)$$

where  $c_0$  and  $c_1$  are the MUSIQ scores of the two input frames,  $t \in [0, 1]$  denotes the normalized position of the target frame, and  $\gamma \in (0, 1]$  controls the interpolation smoothness. The parameter  $\gamma$  controls the interpolation sensitivity, where a larger  $\gamma$  leads to stricter quality estimation and higher reference quality for intermediate frames.

We further conduct an empirical study to determine the appropriate denoising step  $k$  for each target frame under the quality constraint in Eq. (1). For this analysis, we generate images for a set of scenes using both the diffusion model and the regression model, and then perform refinements starting at different denoising steps  $k \in \{5, 10, 15, 20, 25, 30, 35, 40, 45\}$  within a total of 50 denoising steps. For each generated frame, we compute the MUSIQ score and analyze how perceptual quality changes w.r.t. the regression quality and the refinement depth.

Figure 6a illustrates this relationship, where the  $x$ -axis denotes the ratio between the regression model’s MUSIQ score and the interpolated reference quality, and the  $y$ -axis represents the ratio between the refined output’s quality and that of the full diffusion result. Each curve corresponds to a different starting denoising step  $k$ . The plot is derived from 2000 scenes (2 input frames and 4 target frames each) in the

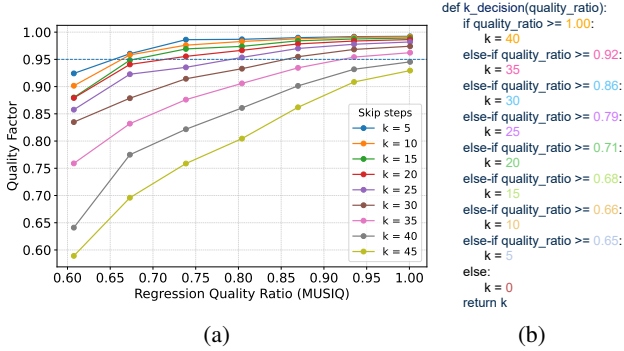


Figure 6. (a) Relationship between regression quality ratio and resulting quality factor across different  $k$ , (b) decision logic for adaptive  $k$  selection based on regression quality.

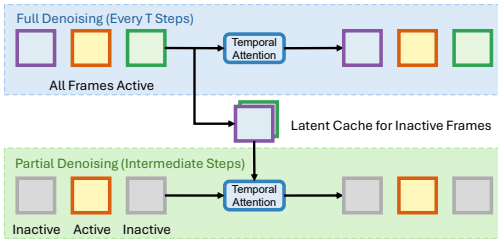


Figure 7. Temporal cache design. We cache temporal attention latents at the first full denoising step  $X_t$ , and reuse them for the next  $(T - 1)$  partial steps for frames not being refined. This preserves temporal consistency while eliminating redundant computation.

RealEstate10K dataset, using SEVA as the diffusion model and MVSplat as the regression model, with the quality factor set to  $\alpha = 0.95$ .

Figure 6b illustrates the  $k$ -decision logic derived from this analysis, which maps the regression quality ratio to the corresponding denoising depth. We set the largest  $k = 40$  to ensure that the final 10 denoising steps are always executed in full, maintaining consistency across different frames and preventing divergence in the final reconstruction quality. These results validate the adaptive scheduling strategy, showing that Sphinx can dynamically balance quality and efficiency across varying scenes and regression qualities.

## 5.2 Temporally Consistent Partial Denoising

To address **Challenge 2**, Sphinx preserves temporal coherence during partial denoising, even when only a subset of frames is refined at each timestep. Conventional diffusion-based NVS models rely on temporal attention layers within transformer blocks to capture motion cues across all frames jointly. However, refining only selected frames breaks this temporal alignment and may introduce flickering or motion discontinuities. Sphinx mitigates this by introducing a latent reuse mechanism that maintains consistent temporal relationships between refined and unrefined frames, ensuring stable motion and coherent scene structure while retaining

the computational advantages of partial denoising.

The U-Net architecture in diffusion-based NVS models typically alternates between convolutional (ResNet) and transformer blocks. The ResNet layers and spatial attention modules operate independently on each frame, capturing intra-frame spatial structure along the height and width dimensions. These components can be safely applied only to frames selected for refinement, as they do not depend on temporal context. In contrast, temporal attention layers capture correspondences across frames to ensure consistency in motion and geometry over time. Naively excluding unrefined frames from these layers disrupts temporal feature aggregation, causing inconsistency in subsequent steps.

To address this, Sphinx introduces a *latent cache* mechanism, as illustrated in Figure 7. Every  $T$  steps, the model performs a full denoising pass over all input and target frames, during which the intermediate latent representations from each temporal attention layer are cached. In the subsequent  $(T - 1)$  partial denoising steps, frames that are not actively refined simply retrieve and reuse these cached latents, enabling temporal attention to maintain full temporal context without recomputing features. This preserves temporal coherence while significantly reducing redundant computation.

## 5.3 Spatially Selective Refinement

The third component of Sphinx addresses **Challenge 3**, enabling efficient refinement within each frame while maintaining spatial coherence. Instead of uniformly applying diffusion to all pixels, Sphinx performs *spatially selective refinement*: restricting diffusion to regions that exhibit uncertainty or artifacts, such as disoccluded surfaces, motion blur, or areas with low reconstruction confidence. This design ensures that reliable regions remain stable, while uncertain regions receive targeted generative enhancement, significantly improving efficiency without sacrificing quality.

As noted in §4, regression-based initialization can often reconstruct many regions of the scene with satisfactory quality, while other areas remain uncertain or distorted. This presents an opportunity to refine only those regions that require further improvement, rather than applying diffusion uniformly. Therefore, the first problem is to determine which parts of the image should be refined. Sphinx combines two complementary cues for this purpose.

First, **opacity-based confidence**. The regression model, based on a 3D Gaussian rasterizer, outputs a per-pixel opacity map that encodes visibility and reconstruction confidence. Pixels with low opacity correspond to uncertain regions such as occlusion boundaries or missing geometry, and are strong candidates for refinement. Sphinx thresholds this opacity map to create an initial binary confidence mask

that marks unreliable regions.

Second, **blur-based uncertainty**. To capture regions suffering from motion blur or texture degradation, Sphinx employs a Laplacian-based blur detection algorithm. The Laplacian measures intensity variations, so sharp regions with strong edges produce high variance, while blurry regions with smooth transitions yield low variance. Thus, the Laplacian variance serves as an effective reference-free indicator of local sharpness. The resulting blur map is smoothed, normalized, and inverted, followed by Otsu thresholding (Otsu, 1979) to obtain a binary mask where 1 indicates blurry pixels. This process is applied to each target image to produce a per-frame blur mask, which complements the opacity-based mask by detecting visually unreliable regions even when geometry is valid.

The opacity- and blur-based masks are then combined to produce a unified spatial refinement mask. For a batch of target frames, Sphinx stacks these masks to form a 3D binary tensor that identifies low-confidence regions across both space and time. Only pixels within this mask are forwarded to the diffusion model for refinement, while high-confidence areas bypass the partial denoising process entirely.

Applying diffusion selectively introduces challenges in spatial layers, as standard convolutional and attention operations expect dense inputs. Similar to the temporal consistency mechanism (§5.2), Sphinx reuses cached latents from the last full denoising step for unrefined regions to maintain spatial consistency. For efficient sparse convolution, we adopt a block-based processing scheme inspired by SBNNet. Instead of performing gather and scatter operations for each individual pixel, which would negate the computational savings, Sphinx tiles the feature maps into blocks matching the convolution kernel size. Each block is marked for refinement if it contains at least one pixel within the refinement mask. This coarse-grained approach enables batched convolution over selected blocks, amortizing memory and compute overhead while preserving spatial correlation across boundaries. Combining geometric and perceptual cues for region selection, latent reuse for spatial coherence, and block-level sparsity for efficiency, Sphinx achieves high-quality selective refinement.

#### 5.4 Adaptive Performance-Quality Control

Finally, Sphinx incorporates an adaptive control mechanism that dynamically adjusts refinement parameters based on scene content and camera configuration, addressing **Challenge 4**. Different scenes exhibit varying levels of complexity. Additionally, variations in camera intrinsics and extrinsics across datasets affect projection geometry and perceived reconstruction difficulty. To accommodate these factors, Sphinx adapts denoising depth and noise scheduling strategy to each scene. This adaptive decision logic allows

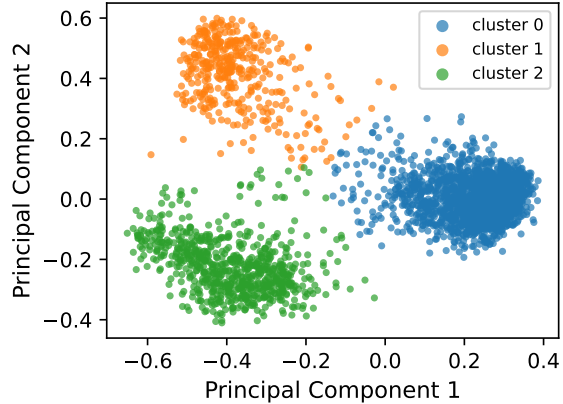


Figure 8. Principle Component Analysis (PCA) visualization of input image embeddings from 3000 scenes across the RE10K, DL3DV and ACID datasets.

the system to offer controllable trade-offs between visual quality and inference speed, ensuring robust performance across diverse real-world conditions.

To address this challenge, Sphinx extends the empirical analysis introduced in §5.1 to derive adaptive  $k$ -decision logic across different scene types and datasets. We conduct experiments on diverse indoor and outdoor scenes to obtain distinct  $k$ -logic mappings that reflect the quality–efficiency trade-off under varying geometric and photometric conditions. To automatically select the appropriate logic during inference, we compute image embeddings for the input views using a pretrained CLIP model (Radford et al., 2021) and perform clustering across all training scenes based on embedding similarity. For each cluster, a specialized  $k$ -logic is derived through empirical analysis.

As shown in Figure 8, the PCA analysis of input image embeddings from 3,000 scenes across the RE10K, DL3DV, and ACID datasets reveals three well-separated clusters. Cluster 0 primarily corresponds to indoor environments, cluster 1 captures long-range landscape views, and cluster 2 represents general outdoor scenes, reflecting distinct visual characteristics that motivate cluster-specific  $k$ -logic designs. During inference, Sphinx first computes the CLIP embedding of the input image, determines its nearest cluster, and applies the corresponding  $k$ -logic to guide noise scheduling and refinement depth.

This design enables scene-aware adaptation of denoising behavior: simple scenes with low visual complexity can use shallower refinement and fewer denoising steps, while complex scenes automatically invoke deeper refinement. By linking visual semantics to adaptive quality control, Sphinx achieves fine-grained regulation of runtime cost without manual tuning, providing a unified and efficient mechanism for balancing quality and performance across diverse inputs.

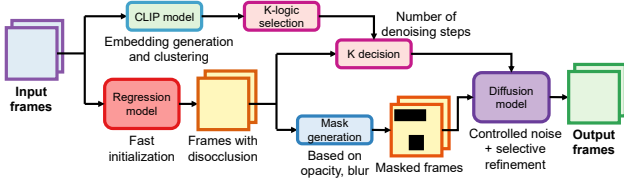


Figure 9. System overview of Sphinx.

## 5.5 System Overview

Figure 9 provides an overview of the Sphinx system, which comprises four key components: (1) a regression model for fast initialization, (2) a CLIP-based module for adaptive  $k$ -logic selection and noise scheduling, (3) a mask generator that locates regions requiring refinement, and (4) a diffusion model for selective denoising with controlled noise. Together, Sphinx enables selective refinement, achieving computational savings while preserving quality.

Algorithm 1 executes the full inference pipeline of Sphinx. Given input views and a set of target poses, the regression model first generates coarse predictions along with opacity estimates, providing a fast initialization. The scene is then encoded using CLIP to determine a cluster index and select the appropriate  $k$ -logic mapping, which translates MUSIQ-based quality ratios into a starting denoising step. A spatial refinement mask is constructed from blur and opacity to identify where refinement is needed. The coarse predictions are encoded into the latent space and noise is injected to move to the selected starting step, after which the diffusion model performs denoising progressively toward the final step, periodically executing full denoising steps to update temporal signals and selectively refining only the regions and frames that require restoration while resampling the inactive ones for synchronization. After completing the denoising schedule, the latents are decoded back into images to produce the final output.

Sphinx provides flexible control over the performance-quality trade-off through tunable runtime parameters. By adjusting the target quality factor, the system dynamically modifies the  $k$ -decision logic to allocate fewer or more denoising steps per request. Similarly, adjusting the opacity or blur thresholds controls the amount of regions selected for refinement, determining how much of the image is processed by diffusion versus skipped to save computation. These knobs allow users to adapt generation quality and computational cost on demand, enabling smooth transitions between high-fidelity and high-throughput operating modes.

## 6 EVALUATION METHODOLOGY

**Datasets and Models.** We evaluate our approach on three representative NVS benchmarks: RealEstate10K (Zhou et al., 2018) (RE10K), ACID (Liu et al., 2021), and

### Algorithm 1 Sphinx Inference

**Require:** Inputs  $I = \{I_0, I_1\}$  with poses; target pose batch  $\Pi = \{\pi_t\}_{t=1}^N$ ; quality  $\alpha$ ; opacity threshold  $\tau_o$ ; cache period  $T$ ; total steps  $S$

**Models:** Regression  $R$ ; Diffusion  $D$ ; CLIP encoder  $E$ ; MUSIQ score  $Q$

**Ensure:** Frames  $\mathbf{Y} \in \mathbb{R}^{N \times H \times W \times C}$

```

// Fast init using Regression model
1:  $(\mathbf{X}, \mathbf{O}) \leftarrow R(I, \Pi)$  {regression outputs: coarse frames and opacity}
// K-logic selection
2:  $e \leftarrow E(I)$ ;  $c \leftarrow \text{cluster}(e)$ ;  $\mathcal{K}_c \leftarrow \text{k\_logic}(c, \alpha)$ 
// Starting step selection
3:  $\hat{Q} \leftarrow Q(\mathbf{X})$  {MUSIQ per item}
4:  $Q^*(t) \leftarrow \text{interp}(Q(I_0), Q(I_1), t/N)$ 
5:  $\mathbf{r} \leftarrow \hat{Q} \oslash Q^*$  {per-item ratio}
6:  $\mathbf{k} \leftarrow \mathcal{K}_c(\mathbf{r})$ ;  $k_{\min} \leftarrow \min(\mathbf{k})$ 
// Spatial masks generation
7:  $\mathbf{B} \leftarrow \text{laplacian\_var}(\mathbf{X})$ 
8:  $\mathbf{M}^{\text{blur}} \leftarrow \text{otsu}(\text{norm}(\mathbf{B}))$  {binary mask from Otsu}
9:  $\mathbf{M}^{\text{op}} \leftarrow \mathbf{1}[\mathbf{O} < \tau_o]$ 
10:  $\mathbf{M} \leftarrow \mathbf{M}^{\text{op}} \vee \mathbf{M}^{\text{blur}}$ 
// Latent initialization & noise injection
11:  $\mathbf{Z}^{(0)} \leftarrow \text{encode}(\mathbf{X})$ 
12:  $\mathbf{Z}^{(k_{\min})} \leftarrow \text{add\_noise}(\mathbf{Z}^{(0)}, k_{\min})$  {noisy latents at start step}
// Partial denoising using Diffusion model
13: for  $u = k_{\min}$  to  $S - 1$  do
14:   if  $u \bmod T = 0$  then
15:      $\mathbf{Z}^{(u+1)} \leftarrow D.\text{full\_step}(\mathbf{Z}^{(u)}, u)$ ;
16:      $\text{cache} \leftarrow \text{store\_temporal}()$ 
17:   else
18:      $\mathbf{A}_u \leftarrow \mathbf{1}[\mathbf{k} \leq u]$  {frames active at step  $u$ }
19:      $\mathbf{Z}_{\mathbf{A}_u}^{(u+1)} \leftarrow D.\text{partial\_step}(\mathbf{Z}_{\mathbf{A}_u}^{(u)}, u, \mathbf{M}_{\mathbf{A}_u}, \text{cache})$ 
20:      $\mathbf{Z}_{\bar{\mathbf{A}}_u}^{(u+1)} \leftarrow \text{add\_noise}(\mathbf{Z}_{\bar{\mathbf{A}}_u}^{(0)}, u+1)$  {inactive frames: resample to step  $u+1$  from clean latents}
21:   end if
22: end for
// Decode latent outputs to final images
23:  $\mathbf{Y} \leftarrow \text{decode}(\mathbf{Z}^{(S)})$ 
24: return  $\mathbf{Y}$ 

```

DL3DV (Ling et al., 2024). RE10K contains diverse indoor scenes with smooth camera motion, widely used for view synthesis and depth learning. ACID focuses on outdoor natural scenes with continuous motion, emphasizing photorealism and long-range consistency. DL3DV includes both indoor and outdoor scenes with dense trajectories and complex lighting, providing a challenging benchmark for generalization. Together, these datasets span diverse visual and geometric conditions for comprehensive evaluation. Our hybrid pipeline integrates both diffusion-based and regression-based models. For the *diffusion stage*, we employ SEVA (Gao et al.) and ViewCrafter (Yu et al., 2025), two state-of-the-art generative NVS models. For the *regression stage*, we adopt MVSplat (Chen et al., 2024) for SEVA and DUST3R (Wang et al., 2024a) for ViewCrafter.

**Baselines.** To assess the effectiveness of our hybrid design, we compare against the following baselines:

- **Diffusion-Only:** Full diffusion-based generation without regression initialization.
- **Regression-Only:** Deterministic regression output without diffusion-based refinement.
- **Sphinx:** The proposed two-stage framework combining regression-based initialization with selective denoising.

**Image Quality Metrics.** We evaluate perceptual quality using the following metrics:

- **PSNR (Netravali & Haskell, 1988):** Measures pixel-level reconstruction fidelity by comparing the mean squared error between generated and ground-truth images.
- **SSIM (Wang et al., 2004):** Captures structural similarity by evaluating luminance, contrast, and structural alignment across image pairs.
- **LPIPS (Zhang et al., 2018):** Estimates perceptual similarity using deep features from pretrained networks that align closely with human visual perception.
- **MUSIQ (Ke et al., 2021):** Provides a no-reference assessment of perceptual and aesthetic quality using a multi-scale vision transformer.

**Implementation Details.** All experiments are implemented in PyTorch (Ansel et al., 2024) and executed on a server equipped with four NVIDIA A40 GPUs (48GB VRAM each). We use a total of 50 diffusion steps for all models, following standard configurations from prior work. For selective refinement, we apply opacity- and blur-based confidence masks to identify regions that require diffusion-based refinement. Pixels with opacity values below 0.5 or identified as blurry are selected for refinement, while the remaining regions are skipped during partial denoising to reduce computation. The input and target resolutions follow the default settings of each model:  $576 \times 576$  for SEVA and  $1024 \times 576$  for ViewCrafter. Both models take two input frames as context. SEVA generates 19 target frames between the inputs, while ViewCrafter produces 23 target frames, following their respective default configurations.

## 7 RESULTS

### 7.1 Latency and Efficiency

Figure 10 compares the performance of Sphinx on SEVA across the RE10K, DL3DV, and ACID datasets under three refinement modes and different quality factors. Each bar shows the mean runtime required to synthesize all target views within a scene, while the blue line represents the 95th percentile (P95) tail latency, the time by which 95% of all scenes complete generation. Sphinx-F (fine-grained) uses the latent cache and reuse mechanism introduced in §5.2; each frame is denoised only at the timesteps it requires, enabling

precise temporal adaptivity. Sphinx-C (coarse-grained) disables latent caching and applies a unified number of denoising steps to all target frames, set to the largest predicted step count among them, which is simpler but less adaptive. Sphinx-S (selective) further reduces computation by spatially skipping denoising in confident regions.

Compared to the full diffusion baseline, Sphinx achieves significant end-to-end latency reductions across all datasets. At a high quality factor of 0.98, Sphinx reaches up to  $1.8 \times$  speedup on the ACID dataset. As the quality factor decreases to 0.90, the speedup further rises to over  $2 \times$  on all three datasets. These results highlight Sphinx’s capability to intelligently reduce denoising workloads while maintaining high visual fidelity, achieving **DG1: adaptively applying denoising to balance fidelity and efficiency**. It is also shown in the figure that across all datasets, the fine-grained mode lowers the P95 tail latency, while the selective mode further substantially reduces it, showing an even greater impact on tail latency compared to its effect on average latency. This indicates that while both modes accelerate inference, *selective refinement is particularly effective at eliminating long-tail cases where certain scenes take disproportionately longer to generate, thereby improving consistency and responsiveness across diverse scene complexities*.

Figure 11 presents similar trends on the ViewCrafter model, where Sphinx achieves over  $1.6 \times$  speedup at a quality factor of 0.9 on the RE10K dataset. The relatively smaller speedup compared to SEVA can be attributed to the lower-quality fast initialization from DUS3R, suggesting that *identifying a stronger regression-based model (e.g., MVSpLat) for initialization is essential to further improve overall efficiency and quality*. Figure 12 shows the distribution of denoising steps required by SEVA and ViewCrafter at a quality factor of 0.95. ViewCrafter requires a larger portion of frames to undergo 30 or more denoising steps, whereas most frames in SEVA complete within 20 steps, demonstrating its strong diffusion prior and rapid convergence. This further underscores the importance of a high-quality initialization, as a stronger starting point can substantially reduce the required denoising workload and improve runtime efficiency.

Within the same quality factor, there is a clear trend that Sphinx-F achieves higher speedup than Sphinx-C, as its finer-grained control avoids redundant denoising for easy frames and saves more computation. When the quality factor is 0.98 and 0.95, Sphinx-S continues to improve speedup due to the additional sparsity introduced by selective refinement. However, the gain is relatively modest because the diffusion model operates in latent space: the image is downsampled by a factor of 8 before entering the U-Net, and the latent features are further gradually downsampled by another factor of 8 within the network. To ensure that all selected pixels are included in the denoising process,

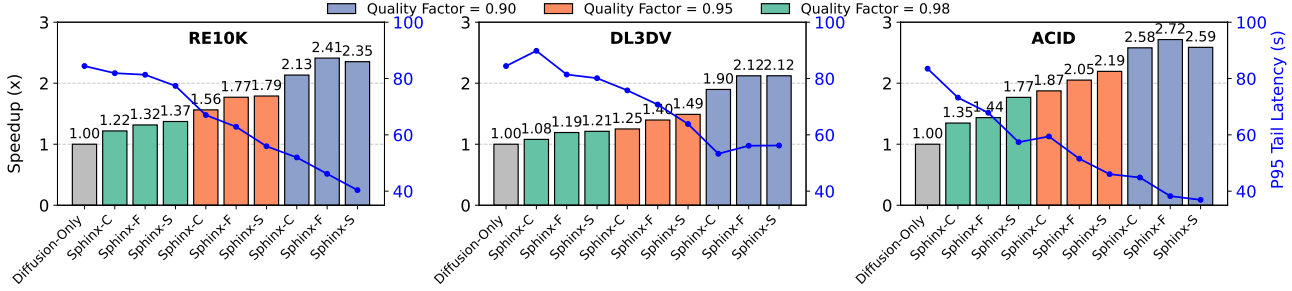


Figure 10. Comparison of SEVA performance across RE10K, DL3DV, and ACID datasets under different quality settings. Each bar represents a refinement mode (Fine, Coarse, Selective), and colors correspond to quality factors 0.98, 0.95, and 0.90.

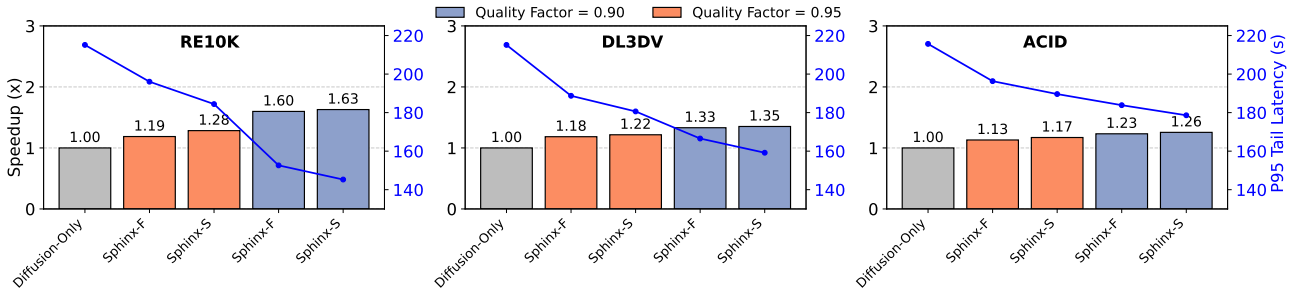


Figure 11. Comparison of ViewCrafter performance across RE10K, DL3DV, and ACID datasets under different quality settings. Each bar represents a refinement mode (Fine, Coarse, Selective), and colors correspond to quality factors 0.98, 0.95, and 0.90.

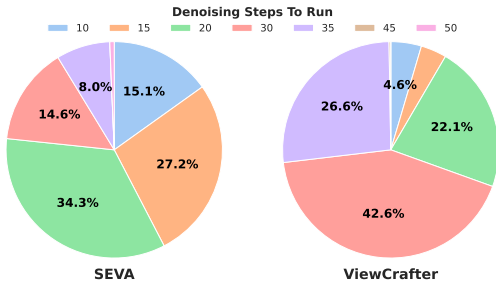


Figure 12. Distribution of frames requiring different numbers of denoising steps for SEVA and ViewCrafter on the RE10K dataset at a quality factor of 0.95.

the confidence mask is downsampled using max-pooling at each layer, which progressively reduces sparsity as the latent representation becomes coarser. When the quality factor decreases to 0.9, the total number of partial denoising steps becomes very small (fewer than 10), limiting the room for selective refinement to provide additional savings. In this case, the overhead of mask generation and latent scatter-gather operations outweighs the computation saved from sparsity, leading to a slight slowdown.

## 7.2 Quality Evaluation

Table 1 presents the quality evaluation of Sphinx on SEVA across the RE10K, DL3DV, and ACID datasets, comparing it against the Diffusion-Only and Regression-Only baselines.

Four standard metrics are reported: MUSIQ, PSNR, SSIM, and LPIPS, where higher MUSIQ, PSNR, and SSIM values and lower LPIPS values indicate better perceptual and structural quality.

Overall, Sphinx demonstrates strong quality retention across all datasets and quality factors. At  $\alpha = 0.98$ , the results remain almost identical to the Diffusion-Only baseline, with differences typically within 1–2%, showing that temporal adaptivity and latent reuse do not harm perceptual fidelity. As the quality factor decreases to  $\alpha = 0.95$  and  $\alpha = 0.90$ , the metrics gradually drop but remain beyond the defined quality threshold, confirming that partial denoising preserves high-level visual realism even under aggressive efficiency settings. This result highlights Sphinx’s ability to satisfy **DG2: ensuring temporal coherence throughout partial denoising**. The selective refinement variant slightly sacrifices perceptual quality, showing negligible drops in MUSIQ and SSIM. This trade-off arises because selective refinement allocates computation only to uncertain regions identified by confidence masks, reducing redundant denoising in confident areas while preserving overall perceptual consistency. This further demonstrates that Sphinx achieves **DG3: enabling spatially selective refinement**. These results collectively show that Sphinx effectively balances between the fidelity of diffusion models with efficiency of regression models.

SEVA		Quality Metrics			
Benchmark	Method	MUSIQ $\uparrow$	PSNR $\uparrow$	SSIM $\uparrow$	LPIPS $\downarrow$
RE10K	Diffusion-Only	63.55	21.28	0.736	0.250
	Sphinx ( $\alpha = 0.98$ )	63.40	21.14	0.737	0.250
	Sphinx ( $\alpha = 0.98$ ) + selective refinement	62.53	21.00	0.737	0.257
	Sphinx ( $\alpha = 0.95$ )	62.46	20.63	0.730	0.262
	Sphinx ( $\alpha = 0.95$ ) + selective refinement	62.10	20.61	0.730	0.265
	Sphinx ( $\alpha = 0.90$ )	60.23	20.21	0.724	0.279
DL3DV	Sphinx ( $\alpha = 0.90$ ) + selective refinement	60.06	20.20	0.725	0.280
	Regression-Only	55.93	20.01	0.726	0.304
	Diffusion-Only	65.43	17.98	0.468	0.379
	Sphinx ( $\alpha = 0.98$ )	63.85	17.12	0.451	0.393
	Sphinx ( $\alpha = 0.98$ ) + selective refinement	64.39	17.13	0.449	0.398
	Sphinx ( $\alpha = 0.95$ )	62.96	16.49	0.439	0.407
ACID	Sphinx ( $\alpha = 0.95$ ) + selective refinement	62.86	16.17	0.431	0.422
	Sphinx ( $\alpha = 0.90$ )	59.96	15.42	0.408	0.455
	Sphinx ( $\alpha = 0.90$ ) + selective refinement	60.39	15.43	0.407	0.460
	Regression-Only	56.59	14.87	0.369	0.517
	Diffusion-Only	64.79	23.86	0.643	0.260
	Sphinx ( $\alpha = 0.98$ )	64.85	23.93	0.651	0.263
NVS	Sphinx ( $\alpha = 0.98$ ) + selective refinement	63.57	23.87	0.657	0.273
	Sphinx ( $\alpha = 0.95$ )	64.17	23.79	0.654	0.268
	Sphinx ( $\alpha = 0.95$ ) + selective refinement	63.39	23.72	0.655	0.274
	Sphinx ( $\alpha = 0.90$ )	63.27	23.62	0.654	0.275
	Sphinx ( $\alpha = 0.90$ ) + selective refinement	63.17	23.60	0.654	0.276
	Regression-Only	62.60	24.60	0.730	0.247

Table 1. SEVA results on RE10K, DL3DV, and ACID. Higher is better for MUSIQ, PSNR, and SSIM; lower is better for LPIPS.

ViewCrafter		Quality Metrics			
Benchmark	Method	MUSIQ $\uparrow$	PSNR $\uparrow$	SSIM $\uparrow$	LPIPS $\downarrow$
RE10K	Diffusion-Only	57.47	15.08	0.574	0.462
	Sphinx ( $\alpha = 0.95$ )	55.74	14.20	0.529	0.486
	Sphinx ( $\alpha = 0.95$ ) + selective refinement	55.18	14.16	0.523	0.489
	Sphinx ( $\alpha = 0.90$ )	52.55	13.78	0.500	0.503
	Sphinx ( $\alpha = 0.90$ ) + selective refinement	52.35	13.76	0.487	0.511
	Regression-Only	40.74	13.77	0.465	0.550
DL3DV	Diffusion-Only	60.56	13.21	0.367	0.566
	Sphinx ( $\alpha = 0.95$ )	58.21	12.83	0.344	0.575
	Sphinx ( $\alpha = 0.95$ ) + selective refinement	58.18	12.81	0.341	0.570
	Sphinx ( $\alpha = 0.90$ )	53.96	12.56	0.336	0.585
	Sphinx ( $\alpha = 0.90$ ) + selective refinement	53.71	12.53	0.329	0.596
	Regression-Only	41.55	12.51	0.306	0.620
ACID	Diffusion-Only	65.35	21.15	0.568	0.345
	Sphinx ( $\alpha = 0.95$ )	61.46	20.08	0.548	0.384
	Sphinx ( $\alpha = 0.95$ ) + selective refinement	61.17	20.03	0.546	0.386
	Sphinx ( $\alpha = 0.90$ )	59.43	19.87	0.547	0.388
	Sphinx ( $\alpha = 0.90$ ) + selective refinement	59.51	19.83	0.539	0.395
	Regression-Only	43.41	19.20	0.530	0.445

Table 2. ViewCrafter results on RE10K, DL3DV, and ACID. Higher is better for MUSIQ, PSNR, and SSIM; lower is better for LPIPS.

### 7.3 Navigating the Performance-Quality Trade-off

Figure 13 illustrates the trade-off space between perceptual quality (measured using the MUSIQ score) and average latency, constructed from experimental results using SEVA across the RE10K, DL3DV, and ACID datasets. We plot latency on the x-axis and MUSIQ on the y-axis, where lower latency and higher quality are both desirable. This orientation emphasizes the central objective of Sphinx: achieving faster generation while preserving high perceptual fidelity. The figure aggregates multiple configurations of Sphinx, covering four quality factors (0.85–0.98) and three refinement modes, Sphinx-C (coarse-grained), Sphinx-F (fine-grained), and Sphinx-S (selective), alongside diffusion-only and regression-only baselines. For Sphinx-S in particular, we also evaluate variants that tog-

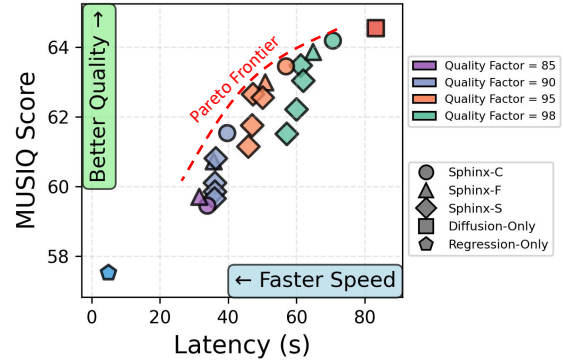


Figure 13. Performance-quality trade-off across different quality factors and method types.

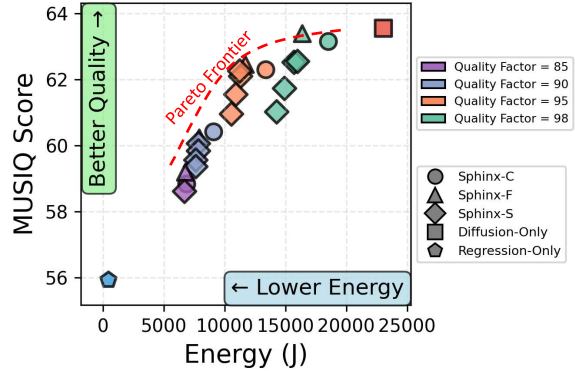


Figure 14. Energy-quality trade-off across different quality factors and method types.

gle blur detection and adjust the opacity threshold, yielding multiple selective-refinement configurations with distinct trade-off behaviors. Overall, the figure demonstrates that by combining regression-based and diffusion-based models, Sphinx achieves our design goal **DG4: adaptive quality-performance control across diverse scenes**. The hybrid design enables flexible navigation along the quality-latency trade-off curve, allowing the system to balance perceptual fidelity and efficiency according to runtime constraints. As a result, *Sphinx* establishes a new **Pareto frontier** for NVS, without needing model training.

### 7.4 Navigating the Energy-Quality Trade-off

Figure 14 presents the trade-off between perceptual quality (MUSIQ) and total energy consumption across multiple quality factors and refinement strategies, using measurements obtained with the Zeus energy-profiling framework (You et al., 2023) alongside SEVA and MVSpIat on the RE10K dataset. Similar to the latency-quality analysis, the ideal operating region lies in the upper-left corner, where quality remains high while energy cost is minimized. In-

terestingly, when the quality factor is high (95% and 98%), the fine-grained refinement mode Sphinx-F achieves **higher perceptual quality at lower energy consumption** than the coarse-grained mode Sphinx-C. The selective refinement mode Sphinx-S further enhances this behavior by enabling fully **adaptive energy–quality control**, dynamically choosing refinement depth to satisfy a given energy budget while still meeting target perceptual thresholds. Together, these results demonstrate that Sphinx provides flexible mechanisms for balancing energy usage and perceptual fidelity across diverse operating conditions.

## 8 RELATED WORKS

Hash3D (Yang et al., 2025) introduces a training-free acceleration method for 3D generation by caching latent features across contiguous frames, but it is limited to object-level scenes with dense inputs. VideoScene (Wang et al., 2025) distills spatiotemporal priors into a lightweight student network for faster video diffusion inference, though it requires additional training and is not directly applicable to hybrid regression–diffusion pipelines. SBNet (Ren et al., 2018) accelerates sparse CNNs through tiling-based sparsity, computing only on active regions but lacking mechanisms for temporal or spatial refinement in diffusion models. Li et al. (Li et al., 2022) propose spatially sparse inference for conditional GANs and diffusion models, but their two-pass design limits efficiency and generality.

## 9 CONCLUSIONS

This paper introduced **Sphinx**, an efficient serving framework for NVS. Sphinx combines regression-based efficiency with diffusion-based fidelity through a hybrid inference pipeline that couples fast regression initialization with selective diffusion refinement. By leveraging adaptive noise scheduling, temporally consistent partial denoising, and spatially selective refinement, it allocates computation where needed. Sphinx achieves an average  $1.8\times$  (up to  $2.2\times$ ) speedup over full diffusion inference with less than 5% perceptual degradation, demonstrating effective and adaptive control of the quality–performance trade-off.

## 10 ACKNOWLEDGMENTS

This work is supported in part by Semiconductor Research Corporation (SRC) as part of the GRC AIHW grant, and AMD AI & HPC Cluster Program.

## REFERENCES

Ansel, J., Yang, E., He, H., Gimelshein, N., Jain, A., Voznesensky, M., Bao, B., Bell, P., Berard, D., Burovski, E., et al. Pytorch 2: Faster machine learning through dynamic

python bytecode transformation and graph compilation. In *Proceedings of the 29th ACM International Conference on Architectural Support for Programming Languages and Operating Systems, Volume 2*, pp. 929–947, 2024.

Berian, A. and Mahalanobis, A. Modern novel view synthesis algorithms: a survey. In *Synthetic Data for Artificial Intelligence and Machine Learning: Tools, Techniques, and Applications III*, volume 13459, pp. 331–337. SPIE, 2025.

Cai, J. and Lu, H. Nerf-based multi-view synthesis techniques: A survey. In *2024 International Wireless Communications and Mobile Computing (IWCMC)*, pp. 208–213. IEEE, 2024.

Charatan, D., Li, S. L., Tagliasacchi, A., and Sitzmann, V. pixelsplat: 3d gaussian splats from image pairs for scalable generalizable 3d reconstruction. In *Proceedings of the IEEE/CVF conference on computer vision and pattern recognition*, pp. 19457–19467, 2024.

Chen, Y., Xu, H., Zheng, C., Zhuang, B., Pollefeys, M., Geiger, A., Cham, T.-J., and Cai, J. Mvsplat: Efficient 3d gaussian splatting from sparse multi-view images. In *European Conference on Computer Vision*, pp. 370–386. Springer, 2024.

Gao, H., Voleti, V., Vasishtha, A., Yao, C.-H., Boss, M., Torr, P., Rupprecht, C., and Jampani, V. Stable virtual camera: Generative view synthesis with diffusion models.

Ke, J., Wang, Q., Wang, Y., Milanfar, P., and Yang, F. Musiq: Multi-scale image quality transformer. In *Proceedings of the IEEE/CVF international conference on computer vision*, pp. 5148–5157, 2021.

Leviathan, Y., Kalman, M., and Matias, Y. Fast inference from transformers via speculative decoding. In *International Conference on Machine Learning*, pp. 19274–19286. PMLR, 2023.

Li, M., Lin, J., Meng, C., Ermon, S., Han, S., and Zhu, J.-Y. Efficient spatially sparse inference for conditional gans and diffusion models. *Advances in neural information processing systems*, 35:28858–28873, 2022.

Ling, L., Sheng, Y., Tu, Z., Zhao, W., Xin, C., Wan, K., Yu, L., Guo, Q., Yu, Z., Lu, Y., et al. D13dv-10k: A large-scale scene dataset for deep learning-based 3d vision. In *Proceedings of the IEEE/CVF Conference on Computer Vision and Pattern Recognition*, pp. 22160–22169, 2024.

Liu, A., Tucker, R., Jampani, V., Makadia, A., Snavely, N., and Kanazawa, A. Infinite nature: Perpetual view generation of natural scenes from a single image. In *Proceedings of the IEEE/CVF International Conference on Computer Vision (ICCV)*, October 2021.

- Liu, S., Yang, M., Xing, T., and Yang, R. A survey of 3d reconstruction: The evolution from multi-view geometry to nerf and 3dgs. *Sensors*, 25(18):5748, 2025.
- Miao, X., Oliaro, G., Zhang, Z., Cheng, X., Wang, Z., Zhang, Z., Wong, R. Y. Y., Zhu, A., Yang, L., Shi, X., Shi, C., Chen, Z., Arfeen, D., Abhyankar, R., and Jia, Z. Specinfer: Accelerating large language model serving with tree-based speculative inference and verification. In *Proceedings of the 29th ACM International Conference on Architectural Support for Programming Languages and Operating Systems, Volume 3*, ASPLOS '24, pp. 932–949. ACM, April 2024. doi: 10.1145/3620666.3651335. URL <http://dx.doi.org/10.1145/3620666.3651335>.
- Mildenhall, B., Srinivasan, P. P., Tancik, M., Barron, J. T., Ramamoorthi, R., and Ng, R. Nerf: Representing scenes as neural radiance fields for view synthesis. In *ECCV*, 2020.
- Netravali, A. N. and Haskell, B. G. *Digital Pictures: Representation, Compression, and Standards*. Springer, 1988.
- Otsu, N. A threshold selection method from gray-level histograms. *IEEE Transactions on Systems, Man, and Cybernetics*, 9(1):62–66, 1979. doi: 10.1109/TSMC.1979.4310076.
- Radford, A., Kim, J. W., Hallacy, C., Ramesh, A., Goh, G., Agarwal, S., Sastry, G., Askell, A., Mishkin, P., Clark, J., Krueger, G., and Sutskever, I. Learning transferable visual models from natural language supervision. *CoRR*, abs/2103.00020, 2021. URL <https://arxiv.org/abs/2103.00020>.
- Ren, M., Pokrovsky, A., Yang, B., and Urtasun, R. Sbnnet: Sparse blocks network for fast inference. In *Proceedings of the IEEE conference on Computer Vision and Pattern Recognition*, pp. 8711–8720, 2018.
- Wang, H., Liu, F., Chi, J., and Duan, Y. Videoscene: Distilling video diffusion model to generate 3d scenes in one step, 2025. URL <https://arxiv.org/abs/2504.01956>.
- Wang, S., Leroy, V., Cabon, Y., Chidlovskii, B., and Revaud, J. Dust3r: Geometric 3d vision made easy. In *Proceedings of the IEEE/CVF Conference on Computer Vision and Pattern Recognition*, pp. 20697–20709, 2024a.
- Wang, Y., Huang, T., Chen, H., and Lee, G. H. Freesplat: Generalizable 3d gaussian splatting towards free view synthesis of indoor scenes. *Advances in Neural Information Processing Systems*, 37:107326–107349, 2024b.
- Wang, Z., Bovik, A., Sheikh, H., and Simoncelli, E. Image quality assessment: from error visibility to structural similarity. *IEEE Transactions on Image Processing*, 13(4):600–612, 2004. doi: 10.1109/TIP.2003.819861.
- Wang, Z., Yuan, Z., Wang, X., Li, Y., Chen, T., Xia, M., Luo, P., and Shan, Y. Motionctrl: A unified and flexible motion controller for video generation. In *ACM SIGGRAPH 2024 Conference Papers*, pp. 1–11, 2024c.
- Watson, D., Saxena, S., Li, L., Tagliasacchi, A., and Fleet, D. J. Controlling space and time with diffusion models. *arXiv preprint arXiv:2407.07860*, 2024.
- Xia, Y., Sharma, D., Yuan, Y., Kundu, S., and Talati, N. Modm: Efficient serving for image generation via mixture-of-diffusion models. In *Proceedings of the 31st ACM International Conference on Architectural Support for Programming Languages and Operating Systems, Volume 1 (ASPLOS '26)*, Pittsburgh, PA, USA, March 2026. Association for Computing Machinery.
- Xu, H., Peng, S., Wang, F., Blum, H., Barath, D., Geiger, A., and Pollefeys, M. Depthspat: Connecting gaussian splatting and depth. In *Proceedings of the Computer Vision and Pattern Recognition Conference*, pp. 16453–16463, 2025.
- Yang, S., Chen, Y., Wang, L., Liu, S., and Chen, Y. Denoising diffusion step-aware models, 2024.
- Yang, X., Liu, S., and Wang, X. Hash3d: Training-free acceleration for 3d generation. In *Proceedings of the Computer Vision and Pattern Recognition Conference*, pp. 21481–21491, 2025.
- You, J., Chung, J.-W., and Chowdhury, M. Zeus: Understanding and optimizing GPU energy consumption of DNN training. In *20th USENIX Symposium on Networked Systems Design and Implementation (NSDI 23)*, pp. 119–139, Boston, MA, April 2023. USENIX Association. ISBN 978-1-939133-33-5. URL <https://www.usenix.org/conference/nsdi23/presentation/you>.
- You, M., Zhu, Z., Liu, H., and Hou, J. Nvs-solver: Video diffusion model as zero-shot novel view synthesizer. In *International Conference on Learning Representations*, 2025.
- Yu, W., Xing, J., Yuan, L., Hu, W., Li, X., Huang, Z., Gao, X., Wong, T.-T., Shan, Y., and Tian, Y. Viewcrafter: Taming video diffusion models for high-fidelity novel view synthesis. *IEEE Transactions on Pattern Analysis and Machine Intelligence*, pp. 1–18, 2025. doi: 10.1109/TPAMI.2025.3613256.

- Zhang, C., Zou, Y., Li, Z., Yi, M., and Wang, H. Transplat: Generalizable 3d gaussian splatting from sparse multi-view images with transformers. In *Proceedings of the AAAI Conference on Artificial Intelligence*, volume 39, pp. 9869–9877, 2025a.
- Zhang, J., Li, Y., Chen, A., Xu, M., Liu, K., Wang, J., Long, X.-X., Liang, H., Xu, Z., Su, H., Theobalt, C., Rupprecht, C., Vedaldi, A., Zhou, K., Liang, P. P., Lu, S., and Zhan, F. Advances in feed-forward 3d reconstruction and view synthesis: A survey, 2025b. URL <https://arxiv.org/abs/2507.14501>.
- Zhang, R., Isola, P., Efros, A. A., Shechtman, E., and Wang, O. The unreasonable effectiveness of deep features as a perceptual metric. In *Proceedings of the IEEE conference on computer vision and pattern recognition*, pp. 586–595, 2018.
- Zhou, T., Tucker, R., Flynn, J., Fyffe, G., and Snavely, N. Stereo magnification: Learning view synthesis using multiplane images. *ACM Trans. Graph. (Proc. SIGGRAPH)*, 37, 2018. URL <https://arxiv.org/abs/1805.09817>.

## A APPENDIX: VISUAL EXAMPLES

Figure 15 presents representative examples of visual quality across different baseline methods. The input to this task consists of two camera frames (*i.e.*, Input Frame 1 and Input Frame 2), and the NVS workload generates multiple intermediate frames between these two input views. For brevity, we display only one generated frame per input scene (each row represents a different scene). Compared to the diffusion baseline, which serves as our quality gold standard, the regression baseline produces inconsistent views with noticeable occlusion artifacts. In contrast, Sphinx with a quality factor of 95% consistently generates output frames with visual quality closely matching the diffusion baseline, while achieving substantially lower computational cost.

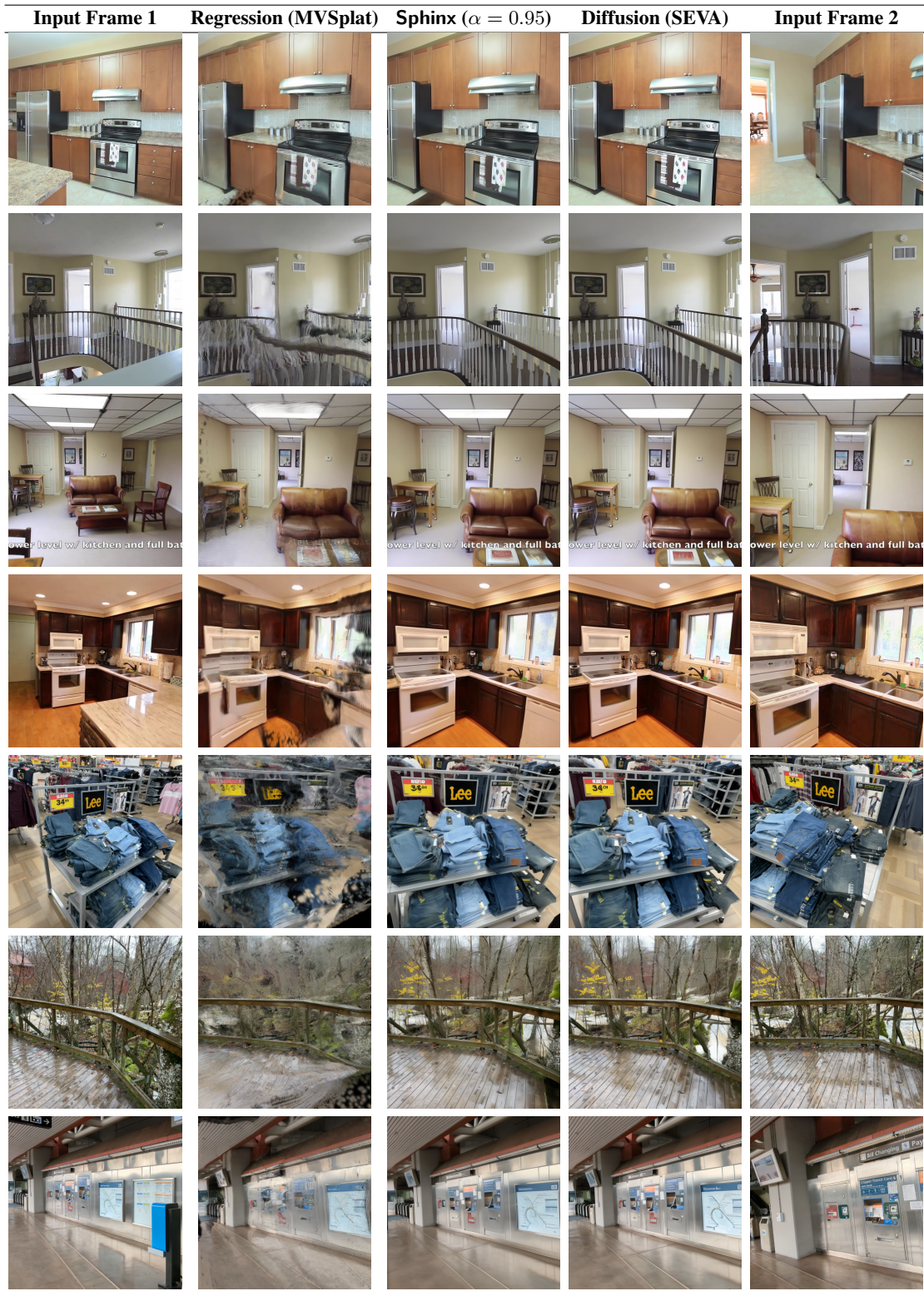


Figure 15. Qualitative comparison of novel view synthesis results across different methods. Each row shows target view generation between two input frames. While many frames are generated between two input frames, this figure only shows **one generated frame** for all baselines (regression, Sphinx, and diffusion) due to space limitation.